# Modulation Engineering: Stimulation Design for Enhanced Kinetic Information from Modulation-Excitation Experiments on Catalytic Systems

*Valentijn De Coster, Nadadur Veeraraghavan Srinath, Parviz Yazdani, Hilde Poelman* and Vladimir V. Galvita*

AUTHOR ADDRESS

Valentijn De Coster – Laboratory for Chemical Technology, Ghent University, Technologiepark 125, B-9052 Ghent, Belgium

Nadadur Veeraraghavan Srinath – Laboratory for Chemical Technology, Ghent University, Technologiepark 125, B-9052 Ghent, Belgium

Parviz Yazdani – Laboratory for Chemical Technology, Ghent University, Technologiepark 125, B-9052 Ghent, Belgium

Hilde Poelman – Laboratory for Chemical Technology, Ghent University, Technologiepark 125, B-9052 Ghent, Belgium

Vladimir V. Galvita – Laboratory for Chemical Technology, Ghent University, Technologiepark 125, B-9052 Ghent, Belgium

AUTHOR INFORMATION

***Corresponding Author**

Hilde Poelman – Laboratory for Chemical Technology, Ghent University, Technologiepark 125, B-9052 Ghent, Belgium; E-mail: Hilde.Poelman@UGent.be

# ABSTRACT

Modulation-excitation (ME) with phase-sensitive detection (PSD) is an emerging strategy to selectively characterize catalytic species that actively participate in a chemical reaction. The commonly applied square-wave (SW) modulations however contain limited frequency content, impeding rigorous kinetic analysis of short-lived reaction intermediates through PSD analysis by considering higher-order harmonics. To overcome this bottleneck, a 'modulation engineering' approach is designed, whereby stimulation shapes with complementary frequency content are superposed onto a base modulation, thus subjecting the system to a more complex frequency pattern in a single experiment. Building on practical and mathematical considerations, this design scheme's feasibility is demonstrated using a superposition of SW and rectangular wave stimulations, applied to $H_2/CO_2$ concentration modulation-excitation X-ray absorption spectroscopy (MEXAS) of a Ni/$MgFeAlO_4$ methane dry reforming (DRM) catalyst at the Fe and Ni K edge. Under redox conditions, PSD evidences Ni↔$Ni^{2+}$ and $Fe^0$↔$Fe^{2+}$↔$Fe^{3+}$ redox events, wherein $Fe^{2+}$↔$Fe^{3+}$ transitions exhibit the faster kinetics, adding insight into this material's redox functionalities under DRM conditions. This approach is extendable to other ME-based characterization techniques and provides a general, time-efficient framework to expand the transient kinetic insights that can be obtained for catalytic systems through ME with PSD.

**KEYWORDS:** X-ray absorption spectroscopy, phase-sensitive detection, Ni-Fe alloy, transient XAS, surface sensitivity

## TOC GRAPHICS

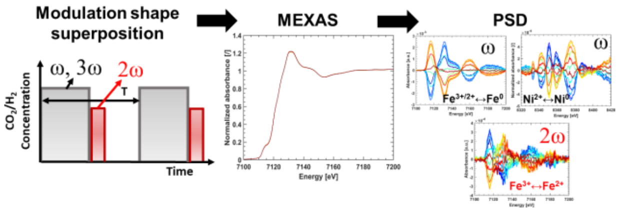

## INTRODUCTION

Understanding the structure of catalysts under reaction conditions through in situ/operando studies is pivotal for the creation of accurate catalyst models and the rational design of novel catalytic materials with optimized performance. Within the field of in situ/operando catalyst characterization, experimental design through modulation-excitation (ME) and a posteriori data analysis via phase-sensitive detection (PSD)[1-3] is particularly attractive, as it yields information with high selectivity towards catalytically 'active' species that could be involved in chemical reactions. In brief, the methodology implies the periodic perturbation of a reaction system (e.g. through reagent concentration, pressure, temperature, pH, …), whilst time-resolved in situ/operando data are acquired. This perturbation or modulation is chosen such that it affects only species of interest. Thus, only these 'target' species will actively respond to the modulation with the same frequency, while 'passive' spectator species and noise do not. A prerequisite for ME is a quasi steady-state, reversible response of the active species, typically established after a transient regime. The former allows averaging the data over a number of periods within this reversible regime, in order to improve the signal-to-noise (S/N) ratio. To extract the active species' response, PSD[3] is applied to the averaged response according to Eq. (1), which transforms the time-resolved data into their phase-resolved counterparts:

$$A_k\left(\varepsilon, \Delta\phi_k^{PSD}\right) = \frac{2}{T}\int_0^T A(\varepsilon, t)\sin\left(k\omega t + \Delta\phi_k^{PSD}\right) dt \qquad (1)$$

where $A(\varepsilon, t)$ is the response measured as a function of time t and an independent variable $\varepsilon$, e.g. energy, $T$ is the modulation period (in s), ω is the (angular) frequency of the stimulation (= 2π/T). $k$ is the demodulation index, an integer with value 1, 2, 3, …, $\Delta\phi_k^{PSD}$ is the demodulation phase angle corresponding to demodulation $k\omega$, and $A_k(\varepsilon, \Delta\phi_k^{PSD})$ are the phase-resolved data of $A(\varepsilon, t)$. A rigorous mathematical background of Eq. (1) is reported elsewhere[2]. In brief, the phase-resolved data represent only contributions that have followed the stimulation with frequency $k\omega$. Passive and noise contributions are eliminated, thereby yielding the selective detection of active species with high S/N ratio. Moreover, since $\Delta\phi_k^{PSD}$ relates to the phase lag of active species with respect to the applied modulation, analysis of the phase domain allows to differentiate the kinetics of various active species[2, 4-6].

While the principle of ME with PSD was originally designed for sinusoidal stimulations[7], square-wave (SW) modulations[8-9] have predominantly been employed in practice. Particularly for concentration modulation, this relates to the facile implementation of such stimulation shapes through valve switching in feed systems. Moreover, SWs have the benefit of comprising a richer frequency content than sine waves[8-9]. Indeed, Fourier series expansion yields for a SW with amplitude B, period T and equilibrium value $B_0$:

$$SW_T(t) = B_0 + \frac{4}{\pi} B \sum_{i=1}^{\infty} \frac{1}{i} \sin\left(\frac{(2i-1)2\pi t}{T}\right) \tag{2}$$

Hence, the response to a SW modulation with fundamental frequency $\omega$ equals the sum of the individual responses to its frequency components $(2i-1)\omega$. By setting $k = (2i-1)$ in Eq. (1), this allows separating the constituent responses from a single SW experiment[2], as opposed to ME experiments with sinusoidal stimulation, where separate experiments at each of these frequencies would be necessary to obtain equivalent information.

With respect to catalytic studies, the ME with PSD approach has seen use in a wide range of characterization techniques, including Fourier transform infrared (FTIR) spectroscopy[4-6, 10-19], Raman spectroscopy[20], UV-Vis spectroscopy[21-23], X-ray absorption spectroscopy (XAS)[7, 13, 24-30], X-ray emission spectroscopy[31] and X-ray diffraction (XRD)[32-35]. Though in each of these studies some form of square-wave stimulation was applied, PSD with $k > 1$ was hardly considered, mainly due to the lower S/N ratio for these cases compared to $k = 1$[35]. Regarding reported FTIR studies, solely Marchionni and co-workers[29] and Srinivasan et al.[6] examined higher-order harmonics, in the study of $Rh/Al_2O_3$ $NO_x$ reduction catalysts and ethanol dehydration over γ-$Al_2O$, respectively. Similarly, in the case of X-ray techniques, only Marchionni et al.[34-35] employed $k > 1$ in SW-based modulation-excitation XRD studies of $Pd/Al_2O_3$ $CH_4$ oxidation catalysts.

Nevertheless, ME-PSD studies with $k > 1$ are highly interesting from a kinetic point of view. PSD with higher $k$ values enhances the sensitivity towards species with faster kinetics, allowing the detection of short-lived intermediates[6, 29, 35], and thus unparalleled insight into catalytic reaction mechanisms. To facilitate associated future studies, it is desirable to obtain a representative overview of these transients by sampling as many frequency components as possible within a single ME experiment. However, from Eq. (2), the commonly applied SW modulation only probes odd multiples of the fundamental frequency, while even multiples are 'skipped'. To include the latter, an additional experiment would be required, utilizing twice the original modulation period.

In view of these considerations, a novel, lean ME with PSD approach is presented for the targeted study of higher frequency components and the faster kinetic events they represent. The strategy consists in 'engineering' the modulation by superposing different stimulation types[6], such that the resulting modulation of one experiment covers frequency components beyond those of the SW. As proof-of-concept, the methodology is applied to Fe and Ni K edge Quick-XAS (QXAS) data for a $Ni/MgFeAlO_4$ methane dry reforming (DRM) catalyst[36-37].

Though $Ni/MgFeAlO_4$ has proven activity in DRM[36], improvements in its design are necessary to allow this catalyst to rival its noble metal-based counterparts[38]. This requires a fundamental understanding of the interaction of the active Ni and Fe species with the DRM environment. For instance, high-temperature $H_2$ reduction ('activation') of $Ni/MgFeAlO_4$ yields Ni-Fe nanoalloys[36], containing the active sites for DRM, whose performance is affected by the redox functionalities of Ni and Fe[36, 39] through interaction with $H_2/CO_2$ in the DRM environment. While volume-averaged information, probed by 'conventional' hard X-ray techniques like XAS, is invaluable for catalyst optimization, questions related to redox events within the active surface fraction of this specific catalyst remain unanswered. To address this matter, an engineered $CO_2/H_2$ MEXAS study is presented on activated Ni/$MgFeAlO_4$.

This is believed to be the first on-purpose consideration of phase-resolved modulation-excitation XAS (MEXAS) data with $k > 1$. The approach in this study can be extended to other ME-based catalyst characterization techniques and as such provides a general, time-efficient framework to expand the kinetic and mechanistic insights that can be obtained from PSD.

## EXPERIMENTAL SECTION

**Material Synthesis.** A $MgFeAlO_4$ support with a nominal 10wt% Fe content was prepared through coprecipitation of an aqueous solution of $Al(NO_3)_3 \cdot 9H_2O$ (ACS reagent, ≥98%, Sigma-Aldrich), $Mg(NO_3)_2 \cdot 6H_2O$ (≥99%, Sigma-Aldrich) and $Fe(NO_3)_3 \cdot 9H_2O$ (≥99.95%, Sigma-Aldrich), using $NH_4OH$ as precipitating agent[36, 40]. The precipitate was aged for 24 h and subsequently filtered, dried at 120 °C for 15 h, and calcined under flowing air at 800 °C for 3 h, using a heating rate of 2 °C/min.

To minimize size-dependent spread of the envisioned MEXAS results, Ni nanoparticles (NPs), meant to be deposited onto $MgFeAlO_4$, were synthesized via a colloidal synthesis method[41]. The obtained Ni NPs were washed three times using acetone (a.r., 99.5+%, Chem-Lab Analytical) and n-hexane (PESTINORM® Supra Trace, ≥99%; VWR Chemicals) as non-solvent and solvent, respectively. The washed NPs, redispersed in 5 mL n-hexane, were used to impregnate $MgFeAlO_4$. 300 mg $MgFeAlO_4$ (sieved 100–150 µm fraction) was put to a 20 mL glass vial containing 2 mL n-hexane, after which the Ni NP dispersion was added. The vial was closed and the content was left to sonicate for 15 h. Following impregnation, the vial was opened and sonicated for 3 h at 55 °C to evaporate the excess of solvent. The resulting powder was then dried at 120 °C for 3 h, and finally calcined at 800 °C (3 °C/min) for 1 h. The obtained material is denoted "Ni/$MgFeAlO_4$".

**Ex Situ Material Characterization.** *ICP-OES*. The bulk elemental composition of calcined $MgFeAlO_4$ and Ni/$MgFeAlO_4$ was determined by inductively coupled plasma optical emission spectrometry (ICP-OES; iCAP 7400, Thermo Scientific). Sample dissolution was performed through sodium peroxide fusion of ~100 mg sample.

*XRD*. The crystallographic phases of as prepared $MgFeAlO_4$ and Ni/$MgFeAlO_4$ were determined via XRD using a Kristalloflex D5000 (Cu Kα, λ = 0.154 nm, from Siemens). Powder patterns were collected in a 2θ range from 15° to 80° with a step of 0.02° and a 30 s counting time per angle.

*STEM*. Scanning transmission electron microscopy (STEM) was used to study the nanoscale morphology. Powder samples were deposited on a lacey carbon film supported on a copper grid by immersing this grid into the sample. A Cs corrected JEM-2200FS (JEOL) equipped with a Schottky-type field-emission gun (FEG) was operated at 200 kV.

**Designing a Modulation with Improved Frequency Content.** This work proposes a strategy to design modulations with customizable frequency content. It consists in the superposition of different modulation types/shapes, such that the frequency content of the overall modulation comprises the sum of those of the separate, constituent modulations. In turn, the characterized system will be exposed to all the frequencies of this 'supermodulation', such that the responses corresponding to each frequency can be extracted via PSD[42].

The above approach is demonstrated for a superposition of two modulation types, using a common time-resolved SW with period T, i.e. $SW_T$, as starting point. Since concentration ME is employed in this work, the values of this SW$_T$ are assumed to be positive in the following rationale. This does not affect the general applicability of the approach, as positivity constraints only alter the constant term in Eq. (2), leaving periodic terms -and their frequency components- unaffected.

Since SW$_T$s lack even multiples of the modulation's fundamental frequency, it is preferable to superpose additional modulation types that, for the same fundamental frequency ω, contain frequency components complementing those of the SW$_T$, all while remaining practically feasible. In view of concentration MEXAS, rectangular waves (RWs), are an interesting option. Let RW$_T$ be a time-resolved RW with period T, pulse width τ and amplitude C, defined as:

$$RW_T(t) = \begin{cases} C & 0 < t \leq \tau \\ 0 & \tau < t < T \end{cases} \tag{3}$$

Note that, for τ = T/2, this simplifies to a SW$_T$ with amplitude C and equilibrium value C/2. The frequency content of the RW$_T$ is determined from its Fourier series:

$$RW_T(t) = \frac{a_0}{2} + \sum_{k=1}^{\infty} a_k \cos(\frac{2k\pi t}{T}) + \sum_{k=1}^{\infty} b_k \sin(\frac{2k\pi t}{T}) \tag{4}$$

with Fourier coefficients (τ and T are assumed to be integers):

$$a_0 = \frac{C\,\tau}{T}$$

$$a_k = \frac{sin\left(\frac{2\,\tau\,k\,\pi}{T}\right)\,C}{k\,\pi} \tag{5}$$

$$b_k = \frac{C\left(cos\left(\frac{2\,\tau\,k\,\pi}{T}\right) - 1\right)}{k\,\pi}$$

For simplicity, let T be an integer multiple of τ:

$$\frac{T}{\tau} = n \qquad\qquad (n \in \mathbb{N}_{>0}) \tag{6}$$

then it follows that both $a_k$ and $b_k$ are zero when $k$ is an integer multiple of n (SI section 1):

$$a_k = b_k = 0 \Leftrightarrow k = m \cdot n \qquad (m \in \mathbb{N}_{>0}) \qquad (7)$$

and thus, frequency components $k\omega$ are absent in the $RW_T$ for $k = m \cdot n$. Therefore, n determines the frequency content of the $RW_T$. In practice, this implies that, for a given T, the pulse width $\tau$ of the $RW_T$ determines its frequency content.

To complement the $SW_T$'s frequency content with lacking frequencies via a superposed $RW_T$, the T/τ ratio of the latter should ideally be an uneven number and as large as possible to assure broad, uninterrupted sampling of sequential frequencies. For a given T, this translates into minimizing τ. However, the following aspects should be taken into consideration when choosing this parameter:

- *Settling time*: In the case of concentration ME, settling time is defined as the time needed ('slope') for the gas feed system to achieve a stable, new flow rate, e.g. after valve switching or flow rate set point change in the mass flow controllers. This introduces limits for the minimal value τ; τ should be -at least- three times ('slope 1' + stable value + 'slope 2') this settling time in order to correctly reach the 'excitation state' of the $RW_T$, i.e. when $RW_T(t)$ has reached its set amplitude C.
- *Modulation data sampling time*: In view of the Nyquist-Shannon theorem, at least two data points (e.g. of the imposed flows/concentrations) should be sampled within the superposed modulation, preferably within the excitation state of the $RW_T$ so as to avoid incorrect interpretation. To facilitate analysis of stimulations in a reaction environment, it can further be proposed to make τ an integer multiple of the modulation data sampling time.

Apart from τ, the amplitude C and time of admittance of $RW_T$ must be chosen (SI section 2). Although the former does not determine the presence of frequency components, it affects their amplitude, since these are linearly proportional to C (Eq. (5)). For uneven $k$, contributions of

$RW_T$ will overlap with those of $SW_T$. To avoid dominant behavior of $RW_T$ at those *k* values, in this work, the amplitude of $RW_T$ is chosen to be an order of magnitude lower than that of $SW_T$. As for the admittance time of $RW_T$, this does not affect the frequency components, yet does influence the phase-resolved data following PSD, as explained in detail by König et al.[42]. Regardless of quantitative PSD analysis, an admission time selection may be motivated out of practical implications, as discussed in SI section 2 and Table S1.

**QXAS experiments.** Transmission QXAS measurements were performed at the ROCK beamline[43] of the 2.75 GeV French synchrotron SOLEIL (500 mA ring current, top-up mode). A Si(111) monochromator[44] oscillating at 2 Hz, recorded the Fe and Ni K edges in one scan, covering both X-ray absorption near edge structure (XANES) and extended X-ray fine edge structure (EXAFS) regions. Calibration was assured through the measurement of a Ni foil.

Ex situ measurements were collected for the following reference samples: NiO, Ni foil, $\gamma$-$Fe_2O_3$, $Fe_3O_4$, FeO and Fe foil. In view of in situ measurements, $Ni/MgFeAlO_4$ was ground to powder and 50% diluted with boron nitride. A 5 mm long catalyst bed was inserted in between two quartz wool plugs into a quartz capillary reactor (outer diameter: 1.2 mm, wall thickness: 0.010 mm, length: 115 mm). The capillary reactor was implemented in a dedicated frame, which was connected to gas feed lines (1/16th inch) through Swagelok fittings and positioned in a custom-built radiative heating furnace to reach desired reaction temperatures[45]. Calibrated Brooks mass flow controllers assured a total inlet flow rate of 7 mL/min. Flow rate values were recorded every 3 s.

Prior to concentration MEXAS, the sample was brought into its active state by $H_2$ temperature-programmed reduction ($H_2$-TPR) under 5% $H_2$/He up to 800°C, with a 10°C/min heating rate and a holding time of 30 min. Afterwards, the cell was cooled down under He to 750 °C and redox cycling for ME was initiated. In consideration of the above designed scheme, modulations were implemented according to Figure S1 (motivation in SI section 3). Automated, periodic gas admission was realized through a macro for flow control using the ROCK beamline's MEXAS setup's[45] mass flow controllers. A constant $H_2$ flow rate of 0.5 mL/min was fed and the $CO_2$ and He flow rates were adjusted such that, sequentially, $CO_2/H_2 = 1/1$ (60 s), $CO_2/H_2 = 2/5$ (12 s) and $CO_2/H_2 = 0$ (48 s) were admitted in one period (T = 120 s). 60 periods of MEXAS were performed. Based on the dimensions of the experimental setup, the gas feed delay to the reactor cell was estimated at 27s. Internal and external mass transfer limitations as well as heat transfer limitations could be discarded and assumption of plug flow regime was allowed, resulting in a residence time of ~0.04 s in the 5 mm catalyst bed.

Additionally, a 'blank' MEXAS experiment was performed at room temperature using a fresh "as prepared" sample, wherein SW modulations of 6 vs. 6.5 mL/min He were applied (T = 120 s) for 30 periods.

For the purpose of examining the activated state of the catalyst, $H_2$-TPR was performed a second time, using a fresh sample, after which the temperature was cooled down to room temperature and QXAS data were collected again. All in situ measurements were performed at atmospheric pressure ($p_{atm}$).

### Data Analysis.

*Concentration Modulation Data.* First, registered flow rates of He, $CO_2$ and $H_2$ ($F_i$; i = He, $CO_2$, $H_2$) were converted to their respective partial pressures ($p_i$), using Eq. (8) to relate the sample responses to the concentration nature of the modulations. To visualize the frequency components, data of 10 sequential periods were then subjected to discrete Fourier transformation (DiscFT), using MATLAB's fft function, and the single-sided amplitude spectrum (P1(f); defined in SI section 4.1) was calculated ($f = \omega/(2\pi)$).

$$p_i = \frac{F_i}{F_{He} + F_{CO_2} + F_{H_2}} p_{atm} \tag{8}$$

To verify whether the modulation contained the targeted frequency components, the modulations were simulated using a superposition of a $SW_T$ and a $RW_T$ and the corresponding P1(f) was again calculated. The simulation quality was assessed using the $R^2_{P1(f)}$ residual factor:

$$R^2_{P1(f)} = \frac{\sum_i P1(f_i)^2_{simulated} - P1(f_i)^2_{experimental}}{\sum_i P1(f_i)^2_{experimental}} \tag{9}$$

*QXAS Data.* QXAS data collected during $H_2$-TPR and MEXAS were averaged over 20 and 10 consecutive scans, respectively, to increase the S/N ratio. This resulted in a net time resolution of 10, respectively, 5 s/spectrum. Ex situ spectra and spectra recorded at room temperature of as prepared and reduced $Ni/MgFeAlO_4$ were averaged over 2000 consecutive scans. All averaged data were normalized and aligned using a dedicated Python normalization GUI[46].

EXAFS data analyses were performed using the Artemis software[47]. Model structures of Ni and Fe oxides and metallic compounds were used to fit the Fourier transformed EXAFS data in R space to derive quantitative structural parameters, namely: bond distance (R), coordination number (CN), Debye-Waller factor (DWF), amplitude reduction factor ($S_0^2$) and energy shift ($\Delta E_0$). Additional EXAFS modelling details are given in SI section 4.2.

Linear combination fitting (LCF) of XANES spectra was performed using the Athena software[47]. To estimate the $Fe^0$ and $Ni^0$ content in the reduced sample, Fe and Ni K edge data were analyzed in the energy intervals [7110–7150] eV and [8330–8370] eV, respectively, using metallic Fe ($Ni_3Fe$ alloy[48]) and Ni (Ni foil) references along with the as prepared material as standards. A $Ni_3Fe$ alloy (with Fe in FCC structure) was chosen over Fe foil (with Fe in BCC structure) as $Fe^0$ reference because, upon Ni-Fe alloy formation after reduction, Fe attains an

FCC structure, displaying different XANES features from BCC Fe[49]. Associated LCF goodness of fit parameters are reported in SI section 4.3.

Multivariate curve resolution-alternating least squares (MCR-ALS) was employed to decompose the time-resolved QXAS spectra – both $H_2$-TPR and MEXAS parts – into their constituent pure component spectra and corresponding concentration profiles[50]. MCR-ALS was performed via the MATLAB® toolbox developed by Jaumot et al.[51]. The analyses comprised the full recorded XAS energy range. Constraints for positivity of the concentrations and spectra were imposed, as well as equating the sum of all concentrations to 1. Initial estimates were of the spectral type and provided via the toolbox's built-in PURE estimation method[52], with a 10% allowance of noise contribution. Goodness of fit parameters are defined in SI section 4.4.

Specifically in the case of the MEXAS data, a series of analysis protocols was followed, as represented in Figure S2. For the purpose of PSD, the quasi steady-state (QSS) regime was identified from the MCR-ALS derived concentration profiles of the MEXAS data. To visualize viable frequency components for PSD[53], the P1(f)s were calculated within this QSS regime. Using this information, MEXAS spectra were first averaged into one period over the number of modulation periods within the QSS regime, after which this averaged, time-resolved dataset was subjected to PSD using the *k* values identified from DiscFT. Since the emphasis in this work is on proving the viability of the adapted modulation approach, phase-resolved MEXAS data were interpreted qualitatively by comparison with difference spectra of reference compounds.

## RESULTS AND DISCUSSION

**(Ni/)$MgFeAlO_4$ Characterization.** The metal contents of as prepared $MgFeAlO_4$ and Ni/$MgFeAlO_4$, as determined by ICP-OES, are reported in Table S2. These confirm that the support's Fe content is close to its nominal value of 10 wt% and that the colloidal synthesis protocol yields a Ni loading such that the net Ni/Fe ratio in Ni/$MgFeAlO_4$ is ~1/1. XRD results of the as prepared support (Figure S3) are in accord with prior work[36, 39], and indicate an Fe-substituted $MgAl_2O_4$ spinel (Powder Diffraction File (PDF) 01-071-1238), i.e. with an $AB_2O_4$ structure wherein A = $Mg^{2+}$ and B = $Al^{3+}$ and $Fe^{3+}$. Diffraction patterns for as prepared Ni/$MgFeAlO_4$ consist of contributions of NiO (PDF 00-047-1049) and the aforementioned Fe-substituted $MgAl_2O_4$ spinel. Average NiO crystallite sizes, estimated with the Scherrer equation, amount to 4.3 nm, in good approximation with STEM results (Figure S4). In addition, STEM reveals an overall spherical shape of the deposited Ni NPs, as well as a monodisperse particle size distribution, a result of the colloidal synthesis approach.

XAS data of as prepared Ni/$MgFeAlO_4$ corroborate the above analyses. Fe (Figure S5A) and Ni K edge (Figure S5B) XANES spectra exhibit $Fe^{3+}$ and $Ni^{2+}$ fingerprints, respectively. EXAFS fitting results at both edges (Figure S5C-D; fit parameters in Table S3) attribute these oxidation states to $Fe^{3+}$ in a $MgAl_2O_4$ spinel, partially substituting $Al^{3+}$, and NiO. Notably, the coordination number (CN) of the NiO-related Ni-Ni paths amounts to 6.6±1.4, which is significantly smaller than 12, i.e. the Ni-Ni CN of FCC NiO, further proving the nanoparticulate character of Ni.

Prior to MEXAS, the catalyst was activated via $H_2$-TPR. Upon $H_2$-TPR of Ni/$MgFeAlO_4$, reduction of both Fe and Ni species is evident from changes in white-line intensity and edge position (Figure S6). From MCR-ALS analyses (Figures S7-S8 and related text), reduction of Fe oxide species occurs from 290 °C on, while NiO reduction starts at 490 °C. In line with prior work[36], Fe reduction occurs only partially; LCF analysis of the sample's Fe K edge XANES spectrum recorded at room temperature after the reduction program (Figure S9A) estimates that ~55% achieves an $Fe^0$ state, indicating this fraction segregates out of the spinel phase upon activation, while the remainder is retained within, presumably as $Fe^{3+}$- or $Fe^{2+}$-substituted $MgAl_2O_4$, i.e. $MgFe^{2+}AlO_4$[36, 39, 54]. Similarly, LCF of the material's Ni K edge XANES spectrum after TPR (Figure S9B) finds a contribution of ~84% $Ni^0$. For completeness, it must be mentioned that discrepancies between the LCF fit and experimental data may originate from the bulk references used in the fit, which are not fully representative of the supported nanoparticulate species in the catalyst. Nevertheless, the latter results indicate ~30% deeper Ni reduction than reported by Theofanidis et al.[36] for $Ni/MgFeAlO_4$ with Ni/Fe = 8/5. This could be due to the current higher Fe content (Ni/Fe ~1/1), enhancing the overall Ni-Fe contact such that the closer proximity of Fe may enhance NiO reduction[55]. An alternative explanation for the higher Ni reduction degree could lie in the colloidal synthesis route employed for the deposition of Ni, which is different from the aqueous wet impregnation method, used by Theofanidis et al.[36]. Fe K edge EXAFS modelling of the reduced spectrum (Figure S9C, fit parameters in Table S4) corroborates the presence of $Fe^0$ as well as residual $MgFe^{2+/3+}AlO_4$. Moreover, the analysis elucidates an FCC Fe structure, which originates from Ni-Fe alloy formation[49], proving that segregated Fe interacts with Ni on the support surface and engages in alloy formation, as previously reported for these $Ni/MgFeAlO_4$ materials after $H_2$-TPR[36]. From the Ni K edge EXAFS results, a similar evidence for alloy formation is not easy to discern (Figure S9D), yet mainly $Ni^0$ and only minor Ni-O contributions are found, which are likely located at the support interface[56]. After activation, the material thus consists of $MgFeAlO_4$ with incorporated $Fe^{2+/3+}$, ~16% Ni-O, as well as ~55% metallic Fe and ~84% metallic Ni fractions, which are engaged in alloy formation.

**Concentration Modulations.** The partial pressures of $H_2$, $CO_2$ and He admitted during the MEXAS experiments are shown in Figure 1A. For visualization purposes, only the first 10 minutes of the program are displayed. The temporal profiles of $p_{H2}$ and $p_{CO2}$ closely resemble the envisioned program in Figure S1. However, due to the inertia of the flow control system, the constituent modulation shapes of $p_{CO2}$ are reminiscent of isosceles trapezoids, i.e. with visible ‘slopes’ between setpoint changes, rather than true vertical sides. Additionally, $p_{H2}$

(Figure 1B) exhibits small deviations from the intended constant value. Since these concur along with the slopes in $p_{CO2}$, it is plausible that they are caused by correlated setpoint switches of the mass flow controllers. As $p_{He}$ (Figure 1C) is correlated with $p_{CO2}$ and $p_{H2}$ through Eq. (8), the same artifacts of $p_{CO2}$ and $p_{H2}$ appear in $p_{He}$.

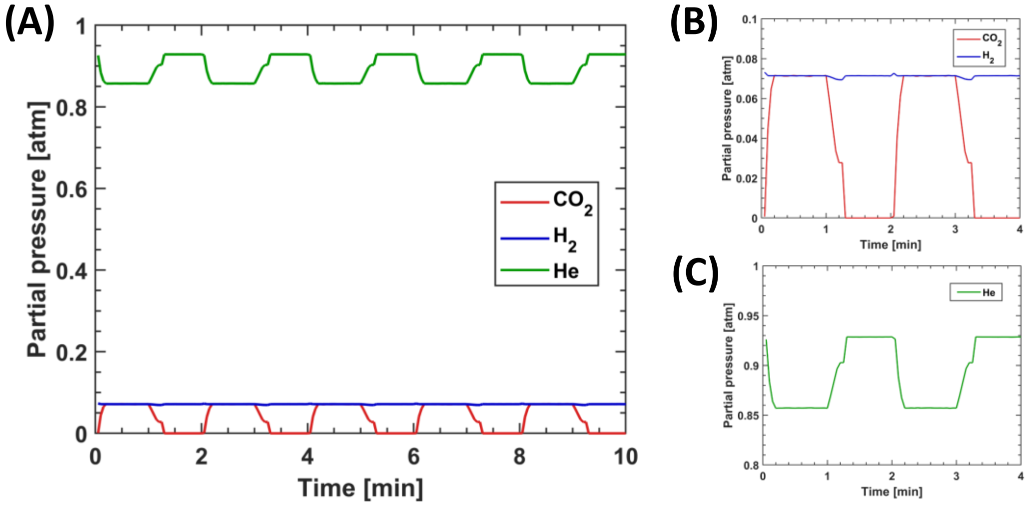

**Figure 1.** (A) Partial pressures of $CO_2$, $H_2$ and He in the feed applied during redox MEXAS experiments (60 s $CO_2/H_2$ = 1/1, 12 s $CO_2/H_2$ = 2/5 and 48 s $CO_2/H_2$ = 0; T = 120 s) of "activated" Ni/$MgFeAlO_4$. For simplicity, only the first 10 minutes of the program are shown. (B) Zoom-in on the $CO_2$ and $H_2$ partial pressures, and (C) on the He partial pressure (first 4 minutes).

To assess the impact of these inertia artifacts on the modulation's frequency content, a separate, blank experiment was performed at room temperature, wherein the total He flow was cycled between 6 and 6.5 mL/min in a SW fashion with a period of 2 min (Figure S10). The resulting modulated flow pattern (Figure S10A) exhibits an isosceles trapezoidal shape, which can serve as case to study the effect of such deviation from SW –and, in extension, RW– shapes. Interestingly, a simulation of this He signal's P1(f) (Figure S10B), using only a SW pattern, yields excellent reproduction of the experimental frequency content ($R^2_{P1(f)}$ = 1.31 $10^{-4}$). The amplitude of P1(f) at 0 $s^{-1}$ represents the average (equilibrium) value of the modulations, which, as expected, equals 6.25. Moreover, all experimental frequency components coincide with those of the SW, while those related to the modulation 'slopes' –which can mathematically be described as a triangular pulse train (SI section 5.7.2, Figure S11)– are absent. Therefore, it is concluded that inertia-related, non-ideal contributions to SWs –and RWs in general– are negligible within the current analysis.

The above reasoning was applied in the simulation of $p_{CO2}$, see Figure 2. Using the SW and RW from the intended modulation program (Figure 2A) achieves good reproduction ($R^2_{P1(f)}$ = 1.2 $10^{-2}$) of the experimental frequency components (Figure 2B). It must be noted that in this frequency pattern, the odd frequencies stem from the SW part of the stimulation. Indeed, a single SW yields only odd frequencies in its experimental P1(f), as is demonstrated by the blank SW He modulation experiment (Figure S10). Because these modulations were performed at RT under He, there is no catalyst response to be seen in the corresponding QXAS data. Nevertheless, with a higher reaction temperature and under a SW of active flows, an actual response can be expected, but only for the odd f, 3f, …, i.e. at the frequencies present in the stimulus, while missing frequencies cannot generate any response.

The experimental frequency pattern in Figure 2B quantitatively proves that, for the used profile, both even and odd multiples of the fundamental frequency are present within the concentration modulation. Herein, odd frequencies arise from the SW part, while the even components can be ascribed to the superposed RW. For completeness, it must be noted that frequency components from this RW are, as intended, one order of magnitude smaller relative to those of the SW.

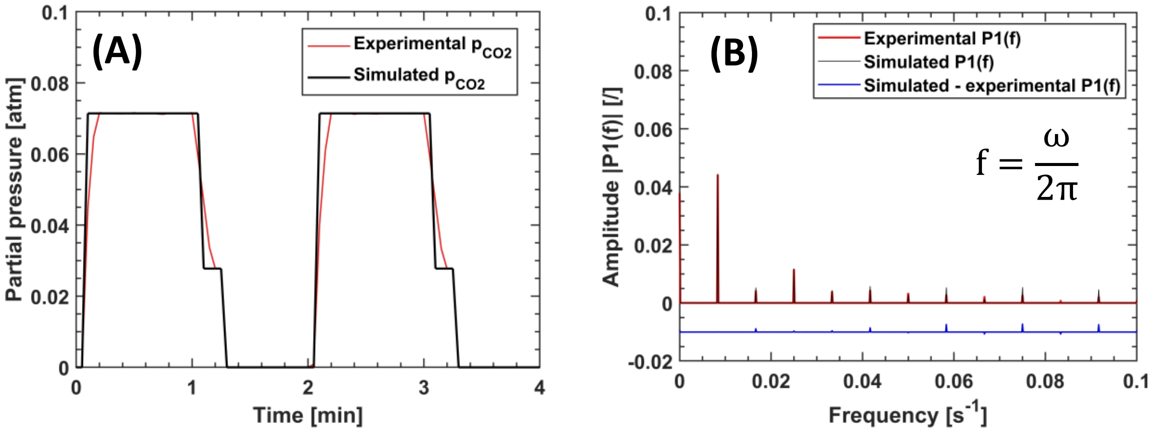

**Figure 2.** (A) Experimental and simulated $CO_2$ partial pressures applied during MEXAS experiments (60 s $CO_2/H_2 = 1/1$ , 12 s $CO_2/H_2 = 2/5$ and 48 s $CO_2/H_2 = 0$; T = 120 s) of "activated" Ni/$MgFeAlO_4$, and (B) corresponding P1(f)s. For simplicity, only the first 4 minutes of the cycling program are shown.

The P1(f)s of $p_{H2}$ and $p_{He}$ are presented in Figure S12. The frequencies of $p_{H2}$ (Figure S12A) are 2 orders of magnitude smaller than the corresponding ones of $p_{CO2}$ (Figure 2B) and thus are negligible in comparison. In other words, fluctuations in the $H_2$ concentration can be disregarded, and the $H_2$ concentration can be approximated as a constant value –as intended. Consequently, the P1(f) of $p_{He}$ (Figure S12B) is –excluding the frequency at 0 $s^{-1}$– quasi-identical to that of $p_{CO2}$, owing to the partial pressures' correlation in Eq. (8).

In summary, the above analysis confirms that frequency components within the redox environment are determined by modulations of the $CO_2$ concentration and that these indeed originate from the imposed wave pattern of the modulation engineering approach.

**MEXAS of activated Ni/MgFeAlO$_4$.** Figure 3 shows the time-resolved Fe and Ni K edge XANES spectra recorded during MEXAS of activated Ni/MgFeAlO$_4$. For Fe, exposure to the redox modulation of Figure 1 induces a transient behavior, wherein first a net though partial oxidation occurs (Figure 3A), after which a seemingly invariant behavior sets in. To examine the re-oxidation extent of the Fe bulk, the Fe K edge spectrum recorded after 60 min into the MEXAS experiment is taken, i.e. in the invariant regime, and compared to those of reference oxide spectra (Figure S13). Its spectral feature at an absorbance of 0.7 (i.e. on the rising edge) is positioned between those of FeO and Fe$_3$O$_4$, while its pre-edge feature intensity lies above that of any oxide reference. Based on this comparison, the Fe re-oxidation likely pertains to an evolution towards Fe$^{2+}$ species, such as FeO$_x$[54], MgFe$^{2+}$AlO$_4$[36, 39, 54] or a combination thereof. On the other hand, no notable changes are observed for Ni K edge data (Figure 3B), suggesting the bulk of Ni retains a Ni$^0$ state under MEXAS conditions. The latter proves the lower affinity of Ni to CO$_2$ under these conditions, compared to Fe.

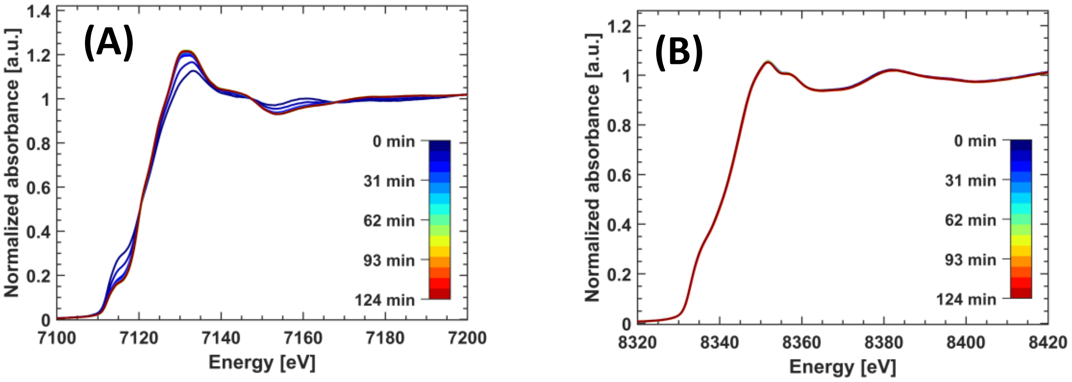

**Figure 3.** Time-resolved XANES spectra recorded at the (A) Fe and (B) Ni K edge during concentration MEXAS experiments of “activated” Ni/MgFeAlO$_4$ at 750 °C.

For the purpose of identifying the QSS regime and suitable frequencies for PSD, MCR-ALS analyses were performed considering 2 components (Figure 4). At the Fe K edge (Figure 4A), the derived Component 1 and Component 2 correspond, respectively, to Fe in the activated catalyst (~57% metallic; Figure S7D) and a more oxidized state. As follows from the concentration profiles (Figure 4B), QSS is achieved after ~78 min, making the last 21 periods viable for PSD. A zoom to the final periods of the concentration profile of spectral Fe Component 2 in this QSS regime is shown in Figure S14B. Only a sinusoidal behavior is observed with a periodicity of 2 min, in line with the modulation period. Higher harmonics are not perceived, reflecting the inertia of the catalyst's Fe species to the broad frequency content within the applied modulation. Theoretically, should the system have been infinitely fast, all of the applied modulation's harmonics should have been present within the concentration profile, such that the latter would have exhibited the same SW+RW shape as the one of the modulation. Subjecting the QSS periods of the concentration profiles to DiscFT (Figure 4C-D) reveals a dominant contribution at 0.0083 $s^{-1}$, i.e. the fundamental modulation frequency (f), with smaller components observed at 0.0166 $s^{-1}$ (2f) and, tentatively, at 0.0247 $s^{-1}$ (3f). DiscFT and P1(f) calculations thus allow determining frequency components that are not perceivable from visual inspection alone. The concentration profiles of both MCR-ALS components share the same amplitudes for all frequencies in their P1(f)s, except for 0 $s^{-1}$, which follows from the imposed boundary condition to equate the sum of all concentrations to 1 in the MCR-ALS analysis. However, the amplitudes of these frequency components decrease in the order f > 2f > 3f, which is in contrast with those calculated from the concentration modulations (Figure 2B), wherein the order was f > 3f > 2f. Typically, redox dynamics occur at ~min time scale[57], making it reasonable to infer that the lower intensity of the 3f component and the overall trend in amplitudes in the P1(f) originate from the limited rate at which Fe species within the QSS react to redox modulations of higher frequency with corresponding sub-minute periods. The absence of higher order harmonics, i.e. above 3f, in the current P1(f) further strengthens this hypothesis.

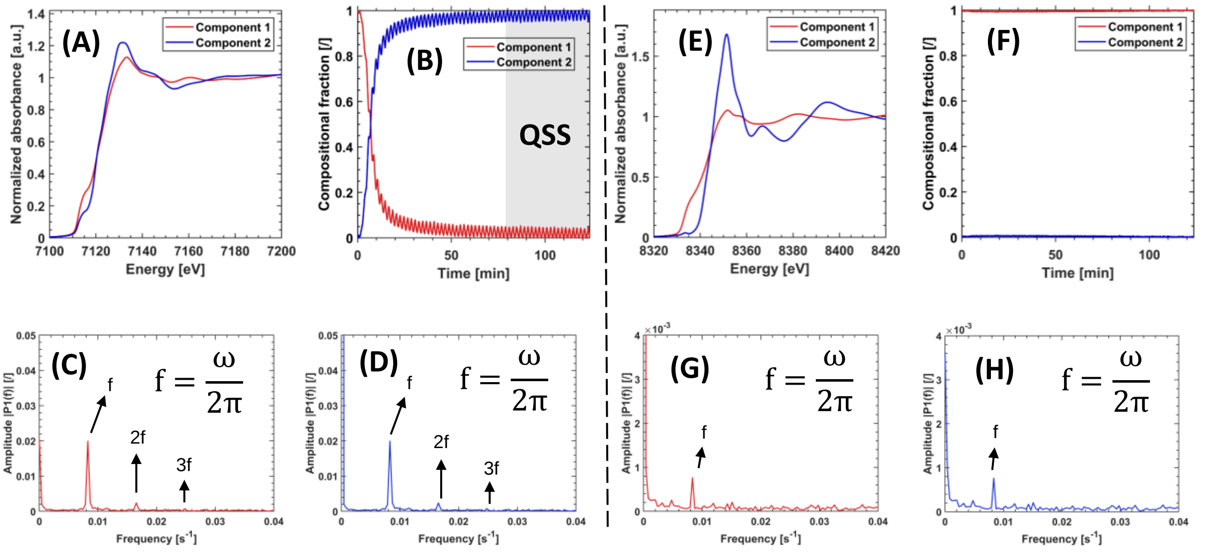

**Figure 4.** (A) XANES component spectra and (B) corresponding concentration profiles derived by MCR-ALS applied to Fe K edge MEXAS data of “activated” Ni/$MgFeAlO_4$ ($R^2$ = 99.9997 %, LOF = 0.2307 % and $\sigma$ = 0.0019). The grey area denotes the QSS regime. (C) P1(f) of the Fe K edge dataset’s QSS concentration profiles of Component 1 and (D) Component 2. (E) XANES component spectra and (F) corresponding concentration profiles derived by CWA-aided MCR-ALS applied to Ni K edge MEXAS data of “activated” Ni/$MgFeAlO_4$ ($R^2$ = 99.9999 %, LOF = 0.0780 % and $\sigma = 7.3104\ 10^{-4}$). (G) P1(f) of the Ni K edge dataset’s QSS concentration profiles of Component 1 and (H) Component 2.

Since the time-resolved Ni K edge MEXAS data are largely invariant, thus impeding analysis via variance-reliant MCR-ALS, a column-wise augmented[58] (CWA) approach was applied wherein the Ni K edge $H_2$-TPR data were appended to the MEXAS data, prior to MCR-ALS. The MCR-ALS results encompassing the full $H_2$-TPR+MEXAS data range are provided in Figure S15. The results in Figure 4E-F correspond to the MEXAS part of these concatenated data. The derived Component 1 and Component 2 (Figure 4E) correspond, respectively, to Ni at the end of $H_2$-TPR (~86% $Ni^0$) and in the as prepared catalyst (NiO). Their concentration profiles (Figure 4F and zoom-in in Figure S14D) further confirm the absence of any electronic or structural change in the bulk of Ni, relative to its activated state. As no transient regime is observed, the last 21 periods of the concentration profiles were taken –cfr. the Fe K edge results– for DiscFT. Notwithstanding the invariant data, the P1(f)s in Figure 4G-H discern a minor component, corresponding to the fundamental modulation frequency, demonstrating the sensitivity of DiscFT and P1(f) in elucidating frequency components, even in noise-dominated concentration profiles (Figure S14D). Higher order harmonics are however not derived, indicating Ni reacts more slowly to the redox modulations than Fe.

To extract the identified frequency contributions from the MEXAS data, PSD was performed. Figure 5 shows the time-resolved Fe K edge XANES spectra from the last recorded 21 periods (the QSS regime) averaged into one period, and their phase-resolved counterparts at demodulation frequencies ω, 2ω and 3ω. In line with MCR-ALS (Figure 4A-B), only subtle changes are visible in the ‘conventional’ XAS spectra within the QSS, as exemplified by the white-line zoom in the inset in Figure 5A. PSD (Figure 5B-D), on the other hand, successfully separates these small periodic contributions from the passive bulk, thereby enhancing the sensitivity towards the fraction of redox-active species. Moreover, equating the demodulation index *k* to 1, 2 or 3 allows filtering out the different frequency components within the PSD data. Higher *k* did not give statistically meaningful results, which validates the P1(f)s in Figure 4C-D. This demonstrates the advantages of PSD over MCR-ALS analysis of the MEXAS data. First, successful MCR-ALS requires notable variance in the analyzed data, e.g. in this case considering both the transient and QSS regime. The latter is not required for PSD, wherein subtle, periodic changes in the data can be extracted from the QSS data alone. Second, MCR-ALS component spectra are inherently ‘bulk’ in nature, wherein passive fractions can easily dominate the minority of redox-active fractions, whereas PSD demodulated spectra selectively represent these active fractions. Finally, utilizing different *k* values in PSD allows separation and identification of events at different frequencies, which is not possible by MCR-ALS. The MCR-ALS-derived spectral components constitute an average result of all frequency components, which thus imposes a – possibly faulty – identity for the events at each of these frequencies.

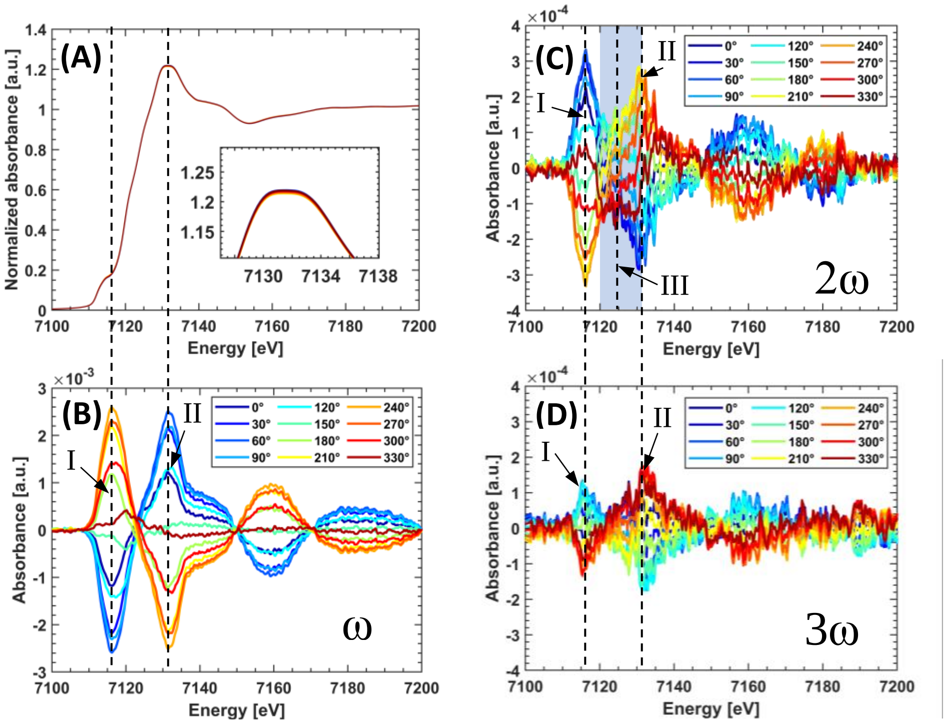

**Figure 5.** (A) Time-resolved Fe K edge XANES spectra, from the final 21 periods averaged into one period, recorded during MEXAS experiments of activated Ni/$MgFeAlO_4$. The inset shows a zoom to the white-line. (B-D) Corresponding phase-resolved spectra at selected phase angles, obtained with demodulation frequencies (B) ω, (C) 2ω and (D) 3ω. Dashed lines and corresponding arrows denote peak positions at (I) 7116, (II) 7132 and (III) 7124 eV in the demodulated spectra; the blue rectangle in (C) indicates the region (7120-7132 eV) of the $Fe^{2+}$-$Fe^{3+}$ feature.

For $k = 1$ (Figure 5B), features at 7116 eV and 7132 eV, corresponding respectively to the Fe K edge XANES pre-edge and white-line, dominate the PSD spectra. The anti-correlation of the two associated amplitudes, as follows from Figure S16A and Figure S16C, suggests these pertain to reversible changes in oxidation state. Comparison of the demodulated spectrum at the phase angle with highest amplitude, i.e. the in-phase angle[2], at 7132 eV (i.e. $\Delta\phi^{PSD} = 60°$, as determined in Figure S16A) with relevant difference spectra (Figure S17) allows identifying the occurring phase changes[13]. These are linked to a combination of $Fe^0 \leftrightarrow Fe^{2+}$ and $Fe^0 \leftrightarrow Fe^{3+}$ redox events occurring in ~1 out of 100 Fe atoms within the sample. Whether $Fe^{3+}$ pertains to $Fe_2O_3$, $Fe_3O_4$, $MgFeAlO_4$, or a combination, cannot be concluded. Even so, this proves that modulating the $CO_2$ concentration induces oxidation state changes between $Fe^0$ and $Fe^{3+}$ for a small fraction of the Fe species. For clarity, due to the anti-correlated nature of the features at

7116 eV and 7132 eV, their corresponding in-phase angles ($\Delta\phi^{PSD}$ = 240°, resp., $\Delta\phi^{PSD}$ = 60°) result in demodulated spectra that differ only in sign from one another. This follows from the sinusoidal term in the PSD equation (Eq. (1)), such that sines of angles that differ by 180° have opposite values. Hence, both in-phase spectra brought forward by $\Delta\phi^{PSD}$ = 240° or $\Delta\phi^{PSD}$ = 60° present the same information content, such that analogous analysis of the demodulated spectrum at the in-phase angle of 7116 eV ($\Delta\phi^{PSD}$ = 240°) would yield identical results as the present analysis of the in-phase spectrum at $\Delta\phi^{PSD}$ = 60°.

Identification is less straightforward for $k > 1$ (Figure 5C-D), as the signal-to-noise ratio decreases with increasing $k$, in line with the amplitude trend observed in the P1(f) (Figure 4C-D). Nevertheless, the same ‘envelopes’ as for $k = 1$ are present, meaning similar redox mechanisms are at play at higher frequencies. In addition, for $k = 2$, a feature centered around ~7124 eV protrudes above noise level, which goes unnoticed in $k = 1$. Examination of this feature’s phase angle dependency (Figure S16E) reveals an in-phase angle at $\Delta\phi^{PSD}$ = 150°, distinct from the in-phase angles of the anti-correlated features at 7116 (Figure S16D) and 7132 eV (Figure S16F), which equate 40° and 220°, respectively. This distinct phase-angle dependency of the feature at 7124 eV indicates that it belongs to phase changes, different from $Fe^{0}\leftrightarrow Fe^{2+}$ and $Fe^{0}\leftrightarrow Fe^{3+}$ transitions. Analysis of the associated in-phase spectral features at 7124 eV (Figure S18) correlates these to $Fe^{2+}\leftrightarrow Fe^{3+}$ transitions. An observation of similar features for $k = 3$ is impeded by the significant noise content.

The demodulated features in Figure 5C-D have true significance, which is confirmed through PSD analysis with $k = 1$ of blank data, i.e. collected at room temperature during the SW He modulations (Figure S10), presented in Figure S19. The latter show absence of periodic changes in the reaction system, i.e. pure noise, with maximum intensities of ~$10^{-5}$: ~8 $10^{-5}$ for Fe and ~7 $10^{-5}$ for Ni K edge data. In contrast, the phase-resolved Fe K edge spectra of the current $CO_2/H_2$

MEXAS experiments at $k = 2$ and $k = 3$ protrude above this noise level, being one order of magnitude higher: 3 $10^{-4}$ for $k = 2$ and 1.4 $10^{-4}$ for $k = 3$.

For posterity, enhancement of the demodulated data for $k = 2$ and $k = 3$ can be realized by recording additional periods, such that averaging over the QSS regime will further reduce the noise content, or by adapting the modulation shape to enhance the amplitude of the associated harmonics within the modulation and, in response, also in the QXAS data.

The fact that $Fe^{2+} \leftrightarrow Fe^{3+}$ redox processes are only observable for $k = 2$, follows from their faster kinetics compared to $Fe^{0} \leftrightarrow Fe^{2+}/Fe^{3+}$, since a higher demodulation index improves sensitivity towards intermediates with shorter lifetime[35]. This is in line with $CO_2$-TPO in situ XRD studies of Ni/$MgFeAlO_4$[37], where the absence of $Fe^{2+}$-associated FeO patterns was attributed to the high reactivity of this intermediate. On the other hand, $Fe^{0} \leftrightarrow Fe^{2+}/Fe^{3+}$ processes can be distinguished up to 3ω, yet their signals dominate at ω, suggesting comparatively slower kinetics. While it is likely that, at 2ω, $Fe^{2+} \leftrightarrow Fe^{3+}$ transitions and $Fe^{0} \leftrightarrow Fe^{2+}/Fe^{3+}$ redox processes concur, these processes exhibit distinct kinetics, as validated by their different in-phase angles at energies of associated changes in Figure 5C ($k = 2$), i.e. $\Delta\phi^{PSD} = 40°$ and 150° (Figure S16D-E) for $Fe^{0} \leftrightarrow Fe^{2+}/Fe^{3+}$ (7116 eV) and $Fe^{2+} \leftrightarrow Fe^{3+}$ (7124 eV), respectively. It must be noted that quantitative kinetic analysis of these phase angles requires dedicated synchronization between the data acquisition and the imposed modulations, which is beyond the scope of this work.

Altogether, qualitative analysis of demodulated Fe K edge data, in part enabled through a priori knowledge of the Ni/$MgFeAlO_4$ system[36], suggests a redox scheme $Fe^{0} \leftrightarrow Fe^{2+} \leftrightarrow Fe^{3+}$ under the imposed modulations, wherein $Fe^{2+} \leftrightarrow Fe^{3+}$ occurs faster than other events. The latter would go unnoticed without analysis at demodulation frequency 2ω, which, in turn, would not have been possible without a related frequency component in the concentration modulations. Hence, this case study delivers experimental validation that the engineering approach to modulation as here proposed, in particular the addition of a RW component to the applied modulation, provides access to additional, otherwise hidden, information of the Ni/$MgFeAlO_4$ system.

Time-resolved Ni K edge XANES data are reported in Figure 6A. Unlike the Fe K edge, periodic changes now go completely unnoticed in the conventional spectra, yet are uncovered by PSD (Figure 6B). In agreement with the P1(f)s in Figure 4G-H, the analysis only gives statistically meaningful results for demodulation frequency ω. The corresponding demodulated spectra consist of multiple features with clear peaks, e.g. at 8333, 8342, 8351, 8359 and 8375 eV. Those at 8333 and 8342 eV fall within the (pre-)edge region, while the ones at 8351 and 8359 eV are located in the white-line region. As the features within these two 'groups' are anti-correlated, it is plausible to relate the observed spectral changes to Ni redox behavior. The demodulated feature below 8333 eV is ascribed to noise, given its low intensity (~$10^{-5}$), similar to that of blank Ni K edge MEXAS data in Figure S19B. The feature at 8375 eV is in-phase with those in the pre-edge region, such that this must also correlate with $Ni^0$ formation. In addition, periodic changes are resolved in the post-edge region (> 8400 eV), which, based on their amplitude, equally correspond to reversible changes within the Ni fine structure. Although re-oxidation of supported Ni by $CO_2$ is not always recognized or considered as such, it has been reported for Ni/$MgFeAlO_4$ by Theofanidis et al.[36] and more recently, examined for Ni/$MgAl_2O_4$ in a dedicated study[56]. Comparison with a NiO-Ni difference spectrum (Figure S20) suggests Ni↔NiO redox behavior occurring in ~1/1000 of Ni atoms. However, the demodulated spectrum deviates considerably from the difference spectrum. This is likely due to physical dissimilarities between the nanoparticulate, incompletely reduced Ni phases in activated Ni/$MgFeAlO_4$ and the pure 'bulk' references, and to possible Ni-Fe (de)alloying with concomitant electronic-structural changes. Furthermore, the phase-resolved spectra represent nanoparticles/nanoalloys wherein only ~1/100 Fe atoms and ~1/1000 Ni atoms participate in redox activities. In contrast, difference (bulk) spectra assume the entire material participates in phase changes – making no distinction between active surface fraction vs. passive bulk.

Regardless of Ni-Fe (de)alloying, Ni re-oxidation is evident under the applied $CO_2$ modulations. In addition, the order of difference in the fraction of Ni atoms (~1/1000) participating in redox events compared to Fe atoms (~1/100), hints at a higher reactivity of $H_2$ with NiO than with $FeO_x$, while the opposite holds true for $CO_2$, resulting in more noticeable redox behavior in Fe/$FeO_x$ compared to Ni/NiO. This corroborates the limited number of frequencies in the Ni K edge MEXAS data (Figure 4G-H), implying that, though present, $H_2$/$CO_2$-redox events in Ni species of activated Ni/$MgFeAlO_4$ are kinetically hindered, adding to their limited net redox activity.

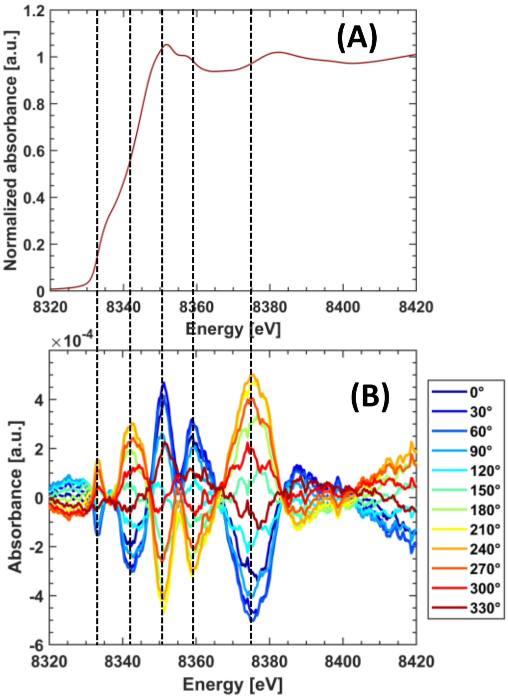

**Figure 6.** (A) Time-resolved Ni K edge XANES spectra, from the final 21 periods averaged into one period, recorded during MEXAS experiments of activated Ni/$MgFeAlO_4$. (B) Corresponding phase-resolved spectra at selected phase angles, obtained with demodulation frequency ω. Dashed lines denote peak features in the demodulated spectra at 8333, 8342, 8351, 8359 and 8375 eV.

Several hypotheses are put forward to explain the relatively slower redox behavior of Ni compared to Fe under the $CO_2/H_2$ modulations. For instance, during the $CO_2$-rich part of the modulation period, Fe might be extracted more easily out the Ni-Fe alloy than Ni[59], after which it is oxidized by $CO_2$[49, 60]. Furthermore, this oxidized Fe could interact with the support matrix, engage in $MgFeO_x$ phasFigurees[39] or even be re-introduced into the $MgFeAlO_4$ matrix altogether. Since Ni redox kinetics are slower, Ni experiences a certain delay in redox behavior relative to such Fe events. A possible explanation is that, after Fe extraction and oxidation, Ni requires metal-metal oxide interface sites to undergo oxidation. The latter provide active sites for $CO_2$ activation[56, 61-62], dissociating it into CO and oxygen species that interact with Ni, ultimately resulting in its oxidation. As such, Ni oxidation occurs at a later instant relative to Fe.

Finally, the $CO_2/H_2$ redox modulations in this study can be adapted to study DRM catalysis. In view of the $CO_2$ and $CH_4$ reagent feed in DRM, $H_2$ applied in the present modulations can be exchanged for $CH_4$ so that the resulting $CO_2/CH_4$ stimulation can be used for DRM-based MEXAS studies. In this reaction, coke formation is a known phenomenon in DRM catalysts, which might prove interesting for examination by MEXAS. For this purpose, the modulation may be further adapted to incorporate a broader frequency content, e.g. by doubling the modulation period (= halving the fundamental frequency) or by adopting a different shape, so as to improve the chances of observing the kinetics of carbon formation and its interaction with $CO_2$ in a DRM-relevant atmosphere.

## CONCLUSIONS

A strategy has been developed to engineer ME experiments for the purpose of enhancing the frequency content in in situ/operando catalyst characterization data in view of a time-efficient approach to analyze transient reaction intermediates. This method consists in the superposition of modulation shapes with complementary frequency components, after which the related frequency components of the net modulation are filtered out by PSD with adapted demodulation frequency $k\omega$. To validate this approach, the superposition of a RW and a SW, with identical period T, was applied to redox ($H_2/CO_2$) Fe and Ni K edge concentration MEXAS of pre-reduced $Ni/MgFeAlO_4$. DiscFT of the applied modulations confirmed that the constituent frequencies arose from the applied modulations. Furthermore, MCR-ALS of time-resolved Fe and Ni K edge spectra successfully predicted statistically significant parameters for PSD, and indicated Fe species exhibit overall faster reactivity ($\omega$, $2\omega$, $3\omega$) to the redox environment than Ni ($\omega$). Corresponding phase-resolved Fe K edge data revealed $Fe^0\leftrightarrow Fe^{2+}\leftrightarrow Fe^{3+}$ transitions, whereby the faster $Fe^{2+}\leftrightarrow Fe^{3+}$ changes were only perceivable due to the $2\omega$ frequency component realized by the modulation engineering approach. Ni, on the other hand, underwent solely $Ni^0\leftrightarrow Ni^{2+}$ transitions. These results add mechanistic insight into how Ni and Fe species in $Ni/MgFeAlO_4$ interact with DRM-related $H_2$ and $CO_2$, allowing the creation of improved catalyst models and materials for $CO_2$ conversion. Finally, this modulation engineering principle, exemplified for but not limited to the case of SW+RW, opens up new perspectives for application to other time-resolved catalyst characterization techniques.

## AUTHOR INFORMATION

### Notes

The authors declare no competing financial interests.

## ASSOCIATED CONTENT

### Supporting Information.

The Supporting Information is available free of charge at https://pubs.acs.org. Rectangular wave frequency content calculations; considerations in choosing $RW_T$ admittance time; MEXAS experiment motivations; single-sided amplitude spectrum explanation; EXAFS modelling, LCF and MCR-ALS goodness of fit parameter details; MEXAS data analysis workflow; ICP-OES results; XRD patterns; STEM of Ni/$MgFeAlO_4$; XANES and EXAFS results for as prepared Ni/$MgFeAlO_4$; MCR-ALS analysis of $H_2$-TPR QXAS data; XANES and EXAFS results for reduced Ni/$MgFeAlO_4$; inertia effects assessments on concentration modulations; P1(f)s of $H_2$ and He partial pressures; supplementary MEXAS MCR-ALS results; supplementary PSD analysis results (PDF).

## ACKNOWLEDGMENTS

V.D.C. acknowledges a personal grant from the Research Fund of Ghent University (BOF; 01D00719). The research leading to these results has been supported by the project CALIPSOplus under Grant Agreement 730872 from the EU Framework Programme for Research and Innovation HORIZON 2020, in supplying financing of subsistence costs for the synchrotron campaign (SOLEIL, proposal 20200555). The authors acknowledge the assistance from the ROCK staff for a smooth beamtime. This work was supported by a public grant overseen by the French National Research Agency (ANR) as part of the “Investissements d’Avenir” program (reference: ANR-10-EQPX-45).

## REFERENCES

1. Müller, P.; Hermans, I. Applications of Modulation Excitation Spectroscopy in Heterogeneous Catalysis. *Ind. Eng. Chem. Res.* **2017,** *56* (5), 1123-1136.
2. Urakawa, A.; Bürgi, T.; Baiker, A. Sensitivity enhancement and dynamic behavior analysis by modulation excitation spectroscopy: Principle and application in heterogeneous catalysis. *Chem. Eng. Sci.* **2008,** *63* (20), 4902-4909.
3. Baurecht, D.; Fringeli, U. P. Quantitative modulated excitation Fourier transform infrared spectroscopy. *Rev. Sci. Instrum.* **2001,** *72* (10), 3782-3792.
4. Bürgi, T.; Baiker, A. In Situ Infrared Spectroscopy of Catalytic Solid−Liquid Interfaces Using Phase-Sensitive Detection:  Enantioselective Hydrogenation of a Pyrone over Pd/$TiO_2$. *J. Phys. Chem. B* **2002,** *106* (41), 10649-10658.
5. Aguirre, A.; Collins, S. E. Selective detection of reaction intermediates using concentration-modulation excitation DRIFT spectroscopy. *Catal. Today* **2013,** *205*, 34-40.
6. Srinivasan, P. D.; Patil, B. S.; Zhu, H.; Bravo-Suárez, J. J. Application of modulation excitation-phase sensitive detection-DRIFTS for in situ/operando characterization of heterogeneous catalysts. *React. Chem. Eng.* **2019,** *4* (5), 862-883.

7. König, C. F. J.; van Bokhoven, J. A.; Schildhauer, T. J.; Nachtegaal, M. Quantitative Analysis of Modulated Excitation X-ray Absorption Spectra: Enhanced Precision of EXAFS Fitting. *J. Phys. Chem. C* **2012,** *116* (37), 19857-19866.
8. Urakawa, A.; Wirz, R.; Bürgi, T.; Baiker, A. ATR-IR Flow-Through Cell for Concentration Modulation Excitation Spectroscopy: Diffusion Experiments and Simulations. *J. Phys. Chem. B* **2003,** *107* (47), 13061-13068.
9. Urakawa, A.; Bürgi, T.; Baiker, A. Kinetic analysis using square-wave stimulation in modulation excitation spectroscopy: Mixing property of a flow-through PM-IRRAS cell. *Chem. Phys.* **2006,** *324* (2), 653-658.
10. Urakawa, A.; Bürgi, T.; Schläpfer, H.-P.; Baiker, A. Simultaneous in situ monitoring of surface and gas species and surface properties by modulation excitation polarization-modulation infrared reflection-absorption spectroscopy: CO oxidation over Pt film. *Chem. Phys.* **2006,** *124* (5), 054717.
11. Maeda, N.; Sano, S.; Mallat, T.; Hungerbühler, K.; Baiker, A. Heterogeneous Asymmetric Hydrogenation of Activated Ketones: Mechanistic Insight into the Role of Alcohol Products by in Situ Modulation-Excitation IR Spectroscopy. *J. Phys. Chem. C* **2012,** *116* (6), 4182-4188.
12. M, A. Á.; Bobadilla, L. F.; Garcilaso, V.; Centeno, M. A.; Odriozola, J. A. $CO_2$ reforming of methane over Ni-Ru supported catalysts: On the nature of active sites by operando DRIFTS study. *J. $CO_2$ Util.* **2018,** *24*, 509-515.
13. Ferri, D.; Kumar, M. S.; Wirz, R.; Eyssler, A.; Korsak, O.; Hug, P.; Weidenkaff, A.; Newton, M. A. First steps in combining modulation excitation spectroscopy with synchronous dispersive EXAFS/DRIFTS/mass spectrometry for in situ time resolved study of heterogeneous catalysts. *PCCP* **2010,** *12* (21), 5634-5646.
14. Alcaraz, M. R.; Aguirre, A.; Goicoechea, H. C.; Culzoni, M. J.; Collins, S. E. Resolution of intermediate surface species by combining modulated infrared spectroscopy and chemometrics. *Anal. Chim. Acta* **2019,** *1049*, 38-46.
15. Have, I. C. t.; Kromwijk, J. J. G.; Monai, M.; Ferri, D.; Sterk, E. B.; Meirer, F.; Weckhuysen, B. M. Uncovering the reaction mechanism behind CoO as active phase for $CO_2$ hydrogenation. *Nat. Commun.* **2022,** *13* (1), 324.
16. Greenaway, A. G.; Marberger, A.; Thetford, A.; Lezcano-González, I.; Agote-Arán, M.; Nachtegaal, M.; Ferri, D.; Kröcher, O.; Catlow, C. R. A.; Beale, A. M. Detection of key transient Cu intermediates in SSZ-13 during $NH_3$-SCR $deNO_x$ by modulation excitation IR spectroscopy. *Chem. Sci.* **2020,** *11* (2), 447-455.
17. Maeda, N.; Meemken, F.; Hungerbühler, K.; Baiker, A. Selectivity-Controlling Factors in Catalytic Methanol Amination Studied by Isotopically Modulated Excitation IR Spectroscopy. *ACS Catal.* **2013,** *3* (2), 219-223.
18. Patil, B. S.; Srinivasan, P. D.; Atchison, E.; Zhu, H.; Bravo-Suárez, J. J. Design, modelling, and application of a low void-volume in situ diffuse reflectance spectroscopic reaction cell for transient catalytic studies. *React. Chem. Eng.* **2019,** *4* (4), 667-678.
19. Chen, M.; Maeda, N.; Baiker, A.; Huang, J. Molecular Insight into Pt-Catalyzed Chemoselective Hydrogenation of an Aromatic Ketone by In Situ Modulation–Excitation IR Spectroscopy. *ACS Catal.* **2012,** *2* (9), 2007-2013.
20. Nuguid, R. J. G.; Ferri, D.; Marberger, A.; Nachtegaal, M.; Kröcher, O. Modulated Excitation Raman Spectroscopy of $V_2O_5/TiO_2$: Mechanistic Insights into the Selective Catalytic Reduction of NO with NH3. *ACS Catal.* **2019,** *9* (8), 6814-6820.
21. Marberger, A.; Ferri, D.; Elsener, M.; Kröcher, O. The Significance of Lewis Acid Sites for the Selective Catalytic Reduction of Nitric Oxide on Vanadium-Based Catalysts. *Angew. Chem. Int. Ed.* **2016,** *55* (39), 11989-11994.
22. Srinivasan, P. D.; Nitz, S. R.; Stephens, K. J.; Atchison, E.; Bravo-Suarez, J. J. Modified Harrick reaction cell for in situ/operando fiber optics diffuse reflectance UV–visible spectroscopic characterization of catalysts. *Appl. Catal. A: Gen.* **2018,** *561*, 7-18.
23. Srinivasan, P. D.; Zhu, H.; Bravo-Suárez, J. J. In situ UV–vis plasmon resonance spectroscopic assessment of oxygen and hydrogen adsorption location on supported gold catalysts. *Molecular Catalysis* **2021,** *507*, 111572.

24. Ferri, D.; Newton, M. A.; Nachtegaal, M. Modulation Excitation X-Ray Absorption Spectroscopy to Probe Surface Species on Heterogeneous Catalysts. *Top. Catal.* **2011,** *54* (16), 1070.
25. Serrer, M.-A.; Gaur, A.; Jelic, J.; Weber, S.; Fritsch, C.; Clark, A. H.; Saraçi, E.; Studt, F.; Grunwaldt, J.-D. Structural dynamics in Ni–Fe catalysts during $CO_2$ methanation – role of iron oxide clusters. *Catal. Sci. Technol.* **2020,** *10* (22), 7542-7554.
26. Gaur, A.; Stehle, M.; Serrer, M. A.; Stummann, M. Z.; La Fontaine, C.; Briois, V.; Grunwaldt, J. D.; Hoj, M. Using Transient XAS to Detect Minute Levels of Reversible S-O Exchange at the Active Sites of $MoS_2$-Based Hydrotreating Catalysts: Effect of Metal Loading, Promotion, Temperature, and Oxygenate Reactant. *ACS Catal.* **2022,** *12* (1), 633-647.
27. Gaur, A.; Hartmann Dabros, T. M.; Høj, M.; Boubnov, A.; Prüssmann, T.; Jelic, J.; Studt, F.; Jensen, A. D.; Grunwaldt, J.-D. Probing the Active Sites of $MoS_2$ Based Hydrotreating Catalysts Using Modulation Excitation Spectroscopy. *ACS Catal.* **2019,** *9* (3), 2568-2579.
28. Czioska, S.; Boubnov, A.; Escalera-López, D.; Geppert, J.; Zagalskaya, A.; Röse, P.; Saraçi, E.; Alexandrov, V.; Krewer, U.; Cherevko, S.; Grunwaldt, J.-D. Increased Ir–Ir Interaction in Iridium Oxide during the Oxygen Evolution Reaction at High Potentials Probed by Operando Spectroscopy. *ACS Catal.* **2021,** *11* (15), 10043-10057.
29. Marchionni, V.; Newton, M. A.; Kambolis, A.; Matam, S. K.; Weidenkaff, A.; Ferri, D. A modulated excitation ED-EXAFS/DRIFTS study of hydrothermal ageing of Rh/$Al_2O_3$. *Catal. Today* **2014,** *229*, 80-87.
30. Lawley, C.; Tehrani, Z. P.; Clark, A. H.; Safonova, O. V.; Döbeli, M.; Strocov, V. N.; Schmidt, T. J.; Lippert, T.; Nachtegaal, M.; Pergolesi, D. Protagonists and spectators during photocatalytic solar water splitting with $SrTaO_xN_y$ oxynitride. *J. Mater. Chem. A* **2022,** *10* (5), 2374-2387.
31. Marchionni, V.; Szlachetko, J.; Nachtegaal, M.; Kambolis, A.; Kröcher, O.; Ferri, D. An operando emission spectroscopy study of Pt/$Al_2O_3$ and Pt/$CeO_2$/$Al_2O_3$. *PCCP* **2016,** *18* (42), 29268-29277.
32. Marchionni, V.; Kambolis, A.; Nachtegaal, M.; Kröcher, O.; Ferri, D. High energy X-ray diffraction and IR spectroscopy of Pt/$Al_2O_3$ during CO oxidation in a novel catalytic reactor cell. *Catal. Struct. React.* **2017,** *3* (1-2), 71-78.
33. Ferri, D.; Newton, M. A.; Di Michiel, M.; Chiarello, G. L.; Yoon, S.; Lu, Y.; Andrieux, J. Revealing the Dynamic Structure of Complex Solid Catalysts Using Modulated Excitation X-ray Diffraction. *Angew. Chem.* **2014,** *126* (34), 9036-9040.
34. Marchionni, V.; Nachtegaal, M.; Ferri, D. Influence of CO on Dry $CH_4$ Oxidation on Pd/$Al_2O_3$ by Operando Spectroscopy: A Multitechnique Modulated Excitation Study. *ACS Catal.* **2020,** *10* (8), 4791-4804.
35. Marchionni, V.; Ferri, D.; Kröcher, O.; Wokaun, A. Increasing the Sensitivity to Short-Lived Species in a Modulated Excitation Experiment. *Anal. Chem.* **2017,** *89* (11), 5801-5809.
36. Theofanidis, S. A.; Galvita, V. V.; Poelman, H.; Dharanipragada, N. V. R. A.; Longo, A.; Meledina, M.; Van Tendeloo, G.; Detavernier, C.; Marin, G. B. Fe-Containing Magnesium Aluminate Support for Stability and Carbon Control during Methane Reforming. *ACS Catal.* **2018,** *8*, 5983-5995.
37. Wang, H.; Srinath, N. V.; Poelman, H.; Detavernier, C.; Li, P.; Marin, G. B.; Galvita, V. V. Hierarchical Fe-modified $MgAl_2O_4$ as a Ni-catalyst support for methane dry reforming. *Catal. Sci. Technol.* **2020,** *10* (20), 6987-7001.
38. Pakhare, D.; Spivey, J. A review of dry ($CO_2$) reforming of methane over noble metal catalysts. *Chem. Soc. Rev.* **2014,** *43* (22), 7813-7837.
39. Longo, A.; Theofanidis, S. A.; Cavallari, C.; Srinath, N. V.; Hu, J.; Poelman, H.; Sabbe, M. K.; Sahle, C. J.; Marin, G. B.; Galvita, V. V. What Makes Fe-Modified $MgAl_2O_4$ an Active Catalyst Support? Insight from X-ray Raman Scattering. *ACS Catal.* **2020,** *10* (12), 6613-6622.
40. Dharanipragada, N. V. R. A.; Buelens, L. C.; Poelman, H.; De Grave, E.; Galvita, V. V.; Marin, G. B. Mg–Fe–Al–O for advanced $CO_2$ to CO conversion: carbon monoxide yield vs. oxygen storage capacity. *J. Mater. Chem. A* **2015,** *3*, 16251-16262.
41. Vrijburg, W. L.; van Helden, J. W. A.; van Hoof, A. J. F.; Friedrich, H.; Groeneveld, E.; Pidko, E. A.; Hensen, E. J. M. Tunable colloidal Ni nanoparticles confined and redistributed in mesoporous silica for $CO_2$ methanation. *Catal. Sci. Technol.* **2019,** *9* (10), 2578-2591.

42. König, C. F. J.; Schildhauer, T. J.; Nachtegaal, M. Methane synthesis and sulfur removal over a Ru catalyst probed in situ with high sensitivity X-ray absorption spectroscopy. *J. Catal.* **2013,** *305*, 92-100.
43. Briois, V.; Fontaine, C.; Belin, S.; Barthe, L.; Moreno, T.; Pinty, V.; Carcy, A.; Girardot, R.; Fonda, E. ROCK: the new Quick-EXAFS beamline at SOLEIL. *J. Phys. Conf. Ser.* **2016,** *712*, 012149.
44. Fonda, E.; Rochet, A.; Ribbens, M.; Barthe, L.; Belin, S.; Briois, V. The SAMBA quick-EXAFS monochromator: XAS with edge jumping. *J. Synchrotron Radiat.* **2012,** *19*, 417-424.
45. La Fontaine, C.; Belin, S.; Barthe, L.; Roudenko, O.; Briois, V. ROCK: A Beamline Tailored for Catalysis and Energy-Related Materials from ms Time Resolution to µm Spatial Resolution. *Synchrotron Radiat. News* **2020,** *33* (1), 20-25.
46. Lesage, C.; Devers, E.; Legens, C.; Fernandes, G.; Roudenko, O.; Briois, V. High pressure cell for edge jumping X-ray absorption spectroscopy: Applications to industrial liquid sulfidation of hydrotreatment catalysts. *Catal. Today* **2019,** *336*, 63-73.
47. Ravel, B.; Newville, M. ATHENA, ARTEMIS, HEPHAESTUS: data analysis for X-ray absorption spectroscopy using IFEFFIT. *J. Synchrotron Radiat.* **2005,** *12*, 537-541.
48. Center for Synchrotron Radiation Research and Instrumentation. IXAS XAFS database. http://ixs.iit.edu/database/ (accessed 6 June 2020).
49. Kim, S. M.; Abdala, P. M.; Margossian, T.; Hosseini, D.; Foppa, L.; Armutlulu, A.; van Beek, W.; Comas-Vives, A.; Copéret, C.; Müller, C. Cooperativity and Dynamics Increase the Performance of NiFe Dry Reforming Catalysts. *J. Am. Chem. Soc.* **2017,** *139* (5), 1937-1949.
50. Conti, P.; Zamponi, S.; Giorgetti, M.; Berrettoni, M.; Smyrl, W. H. Multivariate Curve Resolution Analysis for Interpretation of Dynamic Cu K-Edge X-ray Absorption Spectroscopy Spectra for a Cu Doped $V_2O_5$ Lithium Battery. *Anal. Chem.* **2010,** *82* (9), 3629-3635.
51. Jaumot, J.; de Juan, A.; Tauler, R. MCR-ALS GUI 2.0: New features and applications. *Chemom. Intell. Lab. Syst.* **2015,** *140*, 1-12.
52. Jaumot, J.; Gargallo, R.; De Juan, A.; Tauler, R. A graphical user-friendly interface for MCR-ALS: A new tool for multivariate curve resolution in MATLAB. *Chemom. Intell. Lab. Syst.* **2005,** *76*, 101-110.
53. Phal, Y.; Yeh, K.; Bhargava, R. Concurrent Vibrational Circular Dichroism Measurements with Infrared Spectroscopic Imaging. *Anal. Chem.* **2021,** *93* (3), 1294-1303.
54. De Coster, V.; Srinath, N. V.; Theofanidis, S. A.; Pirro, L.; Van Alboom, A.; Poelman, H.; Sabbe, M. K.; Marin, G. B.; Galvita, V. V. Looking inside a Ni-Fe/$MgAl_2O_4$ catalyst for methane dry reforming via Mössbauer spectroscopy and in situ QXAS. *Appl. Catal. B: Environ.* **2022,** *300*, 120720.
55. Unmuth, E. E.; Schwartz, L. H.; Butt, J. B. Iron alloy Fischer-Tropsch catalysts: I. Oxidation-reduction studies of the Fe-Ni system. *J. Catal.* **1980,** *61* (1), 242-255.
56. De Coster, V.; Srinath, N. V.; Yazdani, P.; Poelman, H.; Galvita, V. V. Does $CO_2$ Oxidize Ni Catalysts? A Quick X-ray Absorption Spectroscopy Answer. *J. Phys. Chem. Lett.* **2022**, 7947-7952.
57. Redekop, E. A.; Galvita, V. V.; Poelman, H.; Bliznuk, V.; Detavernier, C.; Marin, G. B. Delivering a Modifying Element to Metal Nanoparticles via Support: Pt–Ga Alloying during the Reduction of Pt/Mg(Al,Ga)$O_x$ Catalysts and Its Effects on Propane Dehydrogenation. *ACS Catal.* **2014,** *4* (6), 1812-1824.
58. Ruckebusch, C.; De Juan, A.; Duponchel, L.; Huvenne, J. P. Matrix augmentation for breaking rank-deficiency: A case study. *Chemom. Intell. Lab. Syst.* **2006,** *80* (2), 209-214.
59. Theofanidis, S. A.; Galvita, V. V.; Sabbe, M.; Poelman, H.; Detavernier, C.; Marin, G. B. Controlling the stability of a Fe–Ni reforming catalyst: Structural organization of the active components. *Appl. Catal. B: Environ.* **2017,** *209*, 405-416.
60. Theofanidis, S. A.; Galvita, V. V.; Poelman, H.; Marin, G. B. Enhanced Carbon-Resistant Dry Reforming Fe-Ni Catalyst: Role of Fe. *ACS Catal.* **2015,** *5* (5), 3028-3039.
61. Foppa, L.; Margossian, T.; Kim, S. M.; Müller, C.; Copéret, C.; Larmier, K.; Comas-Vives, A. Contrasting the Role of Ni/$Al_2O_3$ Interfaces in Water–Gas Shift and Dry Reforming of Methane. *J. Am. Chem. Soc.* **2017,** *139* (47), 17128-17139.

62. Silaghi, M.-C.; Comas-Vives, A.; Copéret, C. $CO_2$ Activation on Ni/$\gamma$–$Al_2O_3$ Catalysts by First-Principles Calculations: From Ideal Surfaces to Supported Nanoparticles. *ACS Catal.* **2016,** *6* (7), 4501-4505.